JACS
JOURNAL OF THE AMERICAN CHEMICAL SOCIETY
pubs.acs.org/JACS
Article

Azo-Bridged Metal–Organic Frameworks with Robust Zr_6-Cluster Nodes: A Dual-Functional Design for Suppressing Polysulfide Shuttling in Lithium–Sulfur Batteries

Wei Meng,[#] Yaoda Wang,[#] Xiaocheng Zhou, Zong-Ju Chen, Yue Zhao, Pei-Chen Zhao,* Shuai Yuan,* Zhong Jin,* and Cheng-Hui Li*

Cite This: https://doi.org/10.1021/jacs.5c16469

ABSTRACT: Lithium–sulfur (Li–S) batteries are considered promising candidates for next-generation energy storage devices because of their ultrahigh theoretical energy density, low cost, and environmental friendliness. However, their practical application is hindered by the shuttle effect of intermediate polysulfides and the sluggish redox kinetics of sulfur cathodes. Herein, we designed and synthesized a 3D metal–organic framework (MOF) by integrating azo-functionalized ligands with Lewis acidic zirconium (Zr)-oxo clusters (namely, Zr-MTAC) and utilized it as a cathode host material for high-performance Li–S batteries. Systematic experimental analysis and density functional theory calculations confirmed that the introduced azo groups possess highly efficient chemical adsorption ability for polysulfides and can serve as electron transport channels to accelerate the redox kinetics of sulfur cathodes. Benefiting from the synergistic effect of azo groups and Zr-oxo clusters, Zr-MTAC promotes the catalytic conversion of polysulfides, enhancing the sulfur utilization and cycling performance of Li–S batteries. Consequently, the composite sulfur cathodes based on Zr-MTAC exhibit superior cycling reversibility, exceptional cycling stability (~700 mAh g^{-1} remaining capacity after 1000 cycles), and improved rate capability. This work highlights the enormous potential of azo-functionalized MOF materials in developing energy storage devices, providing a practical and feasible solution for high-performance Li–S batteries.

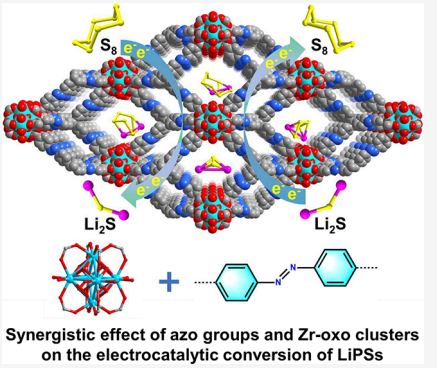

Synergistic effect of azo groups and Zr-oxo clusters on the electrocatalytic conversion of LiPSs

INTRODUCTION

The rapid growth of portable electronics and electric vehicles has driven demand for high-energy-density storage systems,[1−4] while traditional Li-ion batteries (LIBs) have suffered from performance bottlenecks owing to the limited specific capacity of conventional intercalation-type electrodes.[5,6] Lithium–sulfur (Li–S) batteries are recognized as among the most promising energy storage devices, offering a considerable energy density of 2600 Wh kg^{-1} due to the ultrahigh theoretical specific capacity of the sulfur cathode (1675 mAh g^{-1}).[7,8] However, several major technical issues still hinder the practical application of Li–S batteries, including the insulating nature of sulfur and Li_2S, the "shuttle effect" caused by the diffusion of soluble polysulfides, and large volume changes during the lithiation/delithiation process. Consequently, state-of-the-art Li–S batteries still suffer from low sulfur utilization, unsatisfactory cycling lifespan, and sluggish reaction kinetics.[1,8−10] Strenuous efforts have been devoted to resolving these problems to enhance the performance of Li–S batteries, mainly including the physical confinement of sulfur,[11,12] the design of polysulfide-adsorbing host materials,[13−15] Li anode modification for uniform deposition,[16,17] and the development of electrocatalysts to accelerate polysulfide conversion.[18−23] While previous studies have made encouraging progress, it is still challenging to rationally design cathodic host materials for efficient Li–S batteries.

Metal–organic frameworks (MOFs) are crystalline porous materials composed of metal ions or clusters and organic ligands.[24−27] MOFs are well-known for their remarkable characteristics, including tunable compositions, high porosities, and large surface areas. Owing to these physicochemical properties, MOFs have attracted increasing attention for various applications in the fields of gas storage and separation,[28−32] catalysis,[20,33] electrochemical sensors,[34] energy storage devices,[35−37] and many other areas.[38−40] Recent studies have shown that MOFs can be precisely designed for Li–S batteries due to their ordered porosity and stable chemical environments.[15,41−43] Compared with traditional porous carbon/metal oxide host materials, the ordered pores and abundant polar functional groups of MOFs enable efficient

Received: September 18, 2025
Revised: November 7, 2025
Accepted: November 12, 2025

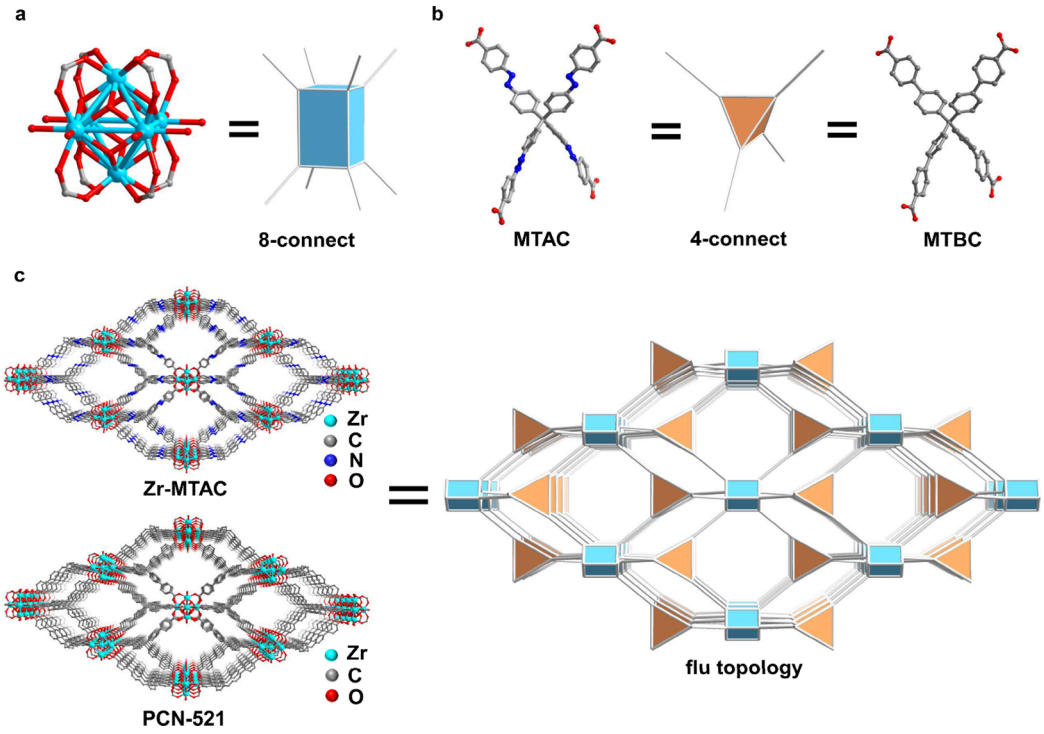

Figure 1. Schematic representation of the design of MOFs. (a) 8-Connected Zr_6 clusters. (b) 4-Connected 4′,4″,4‴,4⁗-methanetetrayltetra (azobenzene)-4-carboxylic acid and 4′,4″,4‴,4⁗-methanetetrayltetrabiphenyl-4-carboxylic acid. (c) Crystal structures of Zr-MTAC and PCN-521 feature a **flu** topology.

polysulfide capture via physical confinement and chemical adsorption. However, despite the great potential of these materials,[12,44−46] there are still limitations in addressing the aforementioned challenges of Li−S batteries. Therefore, new MOF host materials with novel structures and unique properties are needed to improve the Li−S battery performance.

Azo groups (−N=N−), as a vital functional group in chemistry and materials science, have attracted significant interest due to their remarkable properties, including redox activity,[47−50] photoisomerization,[51,52] and Lewis basicity.[53] In particular, aromatic azo molecules have recently garnered significant attention for their potential applications in rechargeable batteries. However, these small azo molecules tend to dissolve substantially in electrolytes and have inferior electrical conductivity, leading to sluggish reaction kinetics and rapid capacity fading.[54−56] In this context, the construction of azo-linked MOFs is expected to yield a novel class of crystalline coordination polymers with fascinating properties. From the perspective of MOF chemistry, incorporating azo functional groups into MOFs can provide not only π-conjugated electronic structures but also rich active sites,[57] making them highly promising for energy storage applications. Inspired by these advancements, we explore the potential of azo-functionalized MOFs as host matrices to effectively suppress the shuttling effect of polysulfides in Li−S batteries.

Herein, we report the design and synthesis of a 3D MOF, named Zr-MTAC, by incorporating azo-functionalized ligands with Zr-oxo clusters, which can serve as a sulfur host material for high-performance Li−S batteries. Meanwhile, an isostructural MOF without azo groups, named PCN-521,[58−60] was synthesized as a control sample. The synthesized Zr-MTAC can efficiently capture polysulfides through both physical confinement and chemical adsorption, in which abundant azo groups act as electron transport channels to facilitate charge transfer during polysulfide conversion, thereby leading to accelerated redox kinetics, improved Coulombic efficiency, and enhanced cycling stability. Moreover, experimental analyses and density functional theory (DFT) calculations demonstrate that the synergistic effect of azo groups and Zr-oxo clusters can effectively reduce the activation energy of polysulfide conversion and accelerate the catalytic conversion of polysulfides. Notably, the Li−S batteries assembled with Zr-MTAC as the cathode host exhibit a higher reversible specific capacity of 1115.6 mAh g^{-1} at 1.0 C, compared with 834.2 mAh g^{-1} for the PCN-521 control sample, and maintain a specific capacity of 699.4 mAh g^{-1} even after 1000 cycles. Moreover, the Zr-MTAC host for the cathode exhibits a favorable rate performance with a specific capacity of 856.5 mAh g^{-1} at 4.0 C. These results demonstrate the great promise of this strategy in promoting the practical application of Li−S batteries.

RESULTS AND DISCUSSION

Synthesis and Characterizations. To investigate the role of azo groups in Li−S batteries, we designed a Zr_6-cluster-based MOF by incorporating azo groups into its structure. In this work, we synthesized a ligand featuring azo linkers, namely, 4′,4″,4‴,4⁗-methanetetrayltetra(azobenzene)-4-carboxylic acid (MTAC). The synthetic route for MTAC is detailed in Schemes S1 and S2 (Supporting Information), with its structure confirmed by ^{1}H and ^{13}C nuclear magnetic resonance (NMR) spectroscopy (Figures S1−S4). The framework of Zr-MTAC was synthesized by reacting $ZrCl_4$ with MTAC under solvothermal conditions in *N,N′*-dimethylformamide (DMF) at 130 °C for 5 days. For comparison, the previously reported PCN-521, constructed

https://doi.org/10.1021/jacs.5c16469
J. Am. Chem. Soc. XXXX, XXX, XXX−XXX

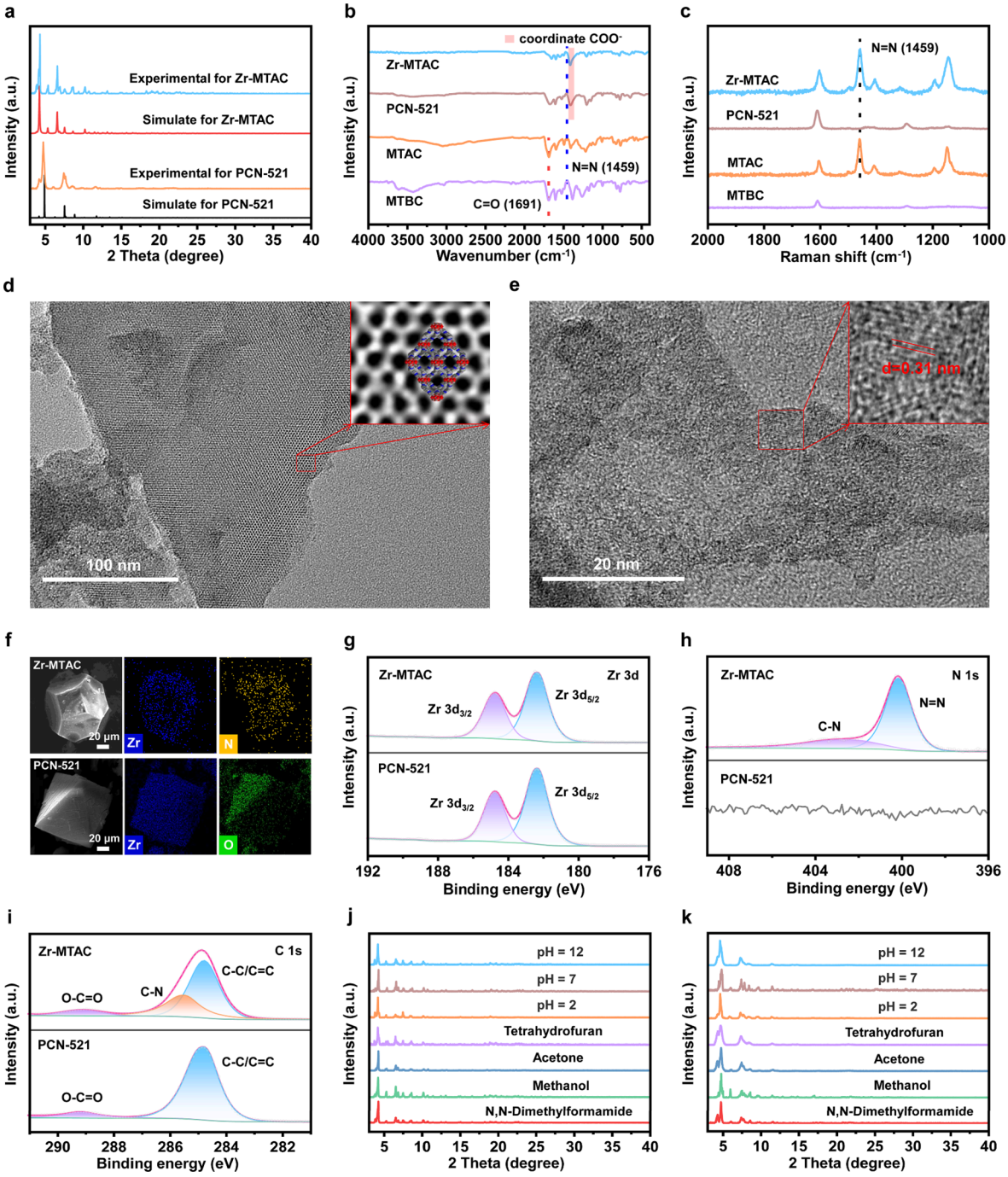

Figure 2. Structural and compositional characterizations of Zr-MTAC and PCN-521. (a) Experimental and simulated PXRD patterns of Zr-MTAC and PCN-521, respectively. (b) FT-IR spectra of Zr-MTAC, PCN-521, and the corresponding synthetic precursors. (c) Raman spectra of Zr-MTAC, PCN-521, and the corresponding synthetic precursors. (d, e) TEM images of Zr-MTAC. (d) The inset shows a perfect coincidence between the TEM-observed structure and the simulated structure of Zr-MTAC. (e) The inset shows the lattice fringes of Zr-MTAC. (f) SEM-EDX mappings of Zr-MTAC and PCN-521. (g–i) High-resolution XPS spectra at (g) Zr 3d, (h) N 1s, and (i) C 1s regions of Zr-MTAC and PCN-521. (j, k) PXRD patterns demonstrating the stability of (j) Zr-MTAC and (k) PCN-521.

using 4′,4″,4‴,4⁗-methanetetrayltetrabiphenyl-4-carboxylic acid (MTBC) ligand, was referenced.[58,60] Single-crystal X-ray diffraction revealed that Zr-MTAC crystallizes in tetragonal space group *I4/m* (Tables S1 and S2). The asymmetric unit of Zr-MTAC contains three-fourths of a Zr^{4+} ion, one-fourth of a $MTAC^{4-}$ linker, one O^{2-} ion, and two water molecules (Figures S5–S7). Topologically, the $[Zr_6(\mu_3\text{-}O)_8(O)_8]^{8-}$ clusters functioned as 8-connected nodes (Figure 1a), while the MTAC or MTBC tetrahedral ligands served as 4-connected nodes (Figure 1b), forming MOFs with the 4,8-connected **flu** topology (Figure 1c). The powder X-ray diffraction (PXRD) patterns of Zr-MTAC and PCN-521 matched well with the simulated patterns derived from their single-crystal structures, confirming the phase purity of the bulk samples (Figure 2a). However, upon solvent removal, Zr-MTAC could undergo gradual phase transition with peak shifts, a phenomenon also reported for other similar Zr-MOFs with **flu** topology.[61] This flexibility was further supported by

https://doi.org/10.1021/jacs.5c16469
J. Am. Chem. Soc. XXXX, XXX, XXX−XXX

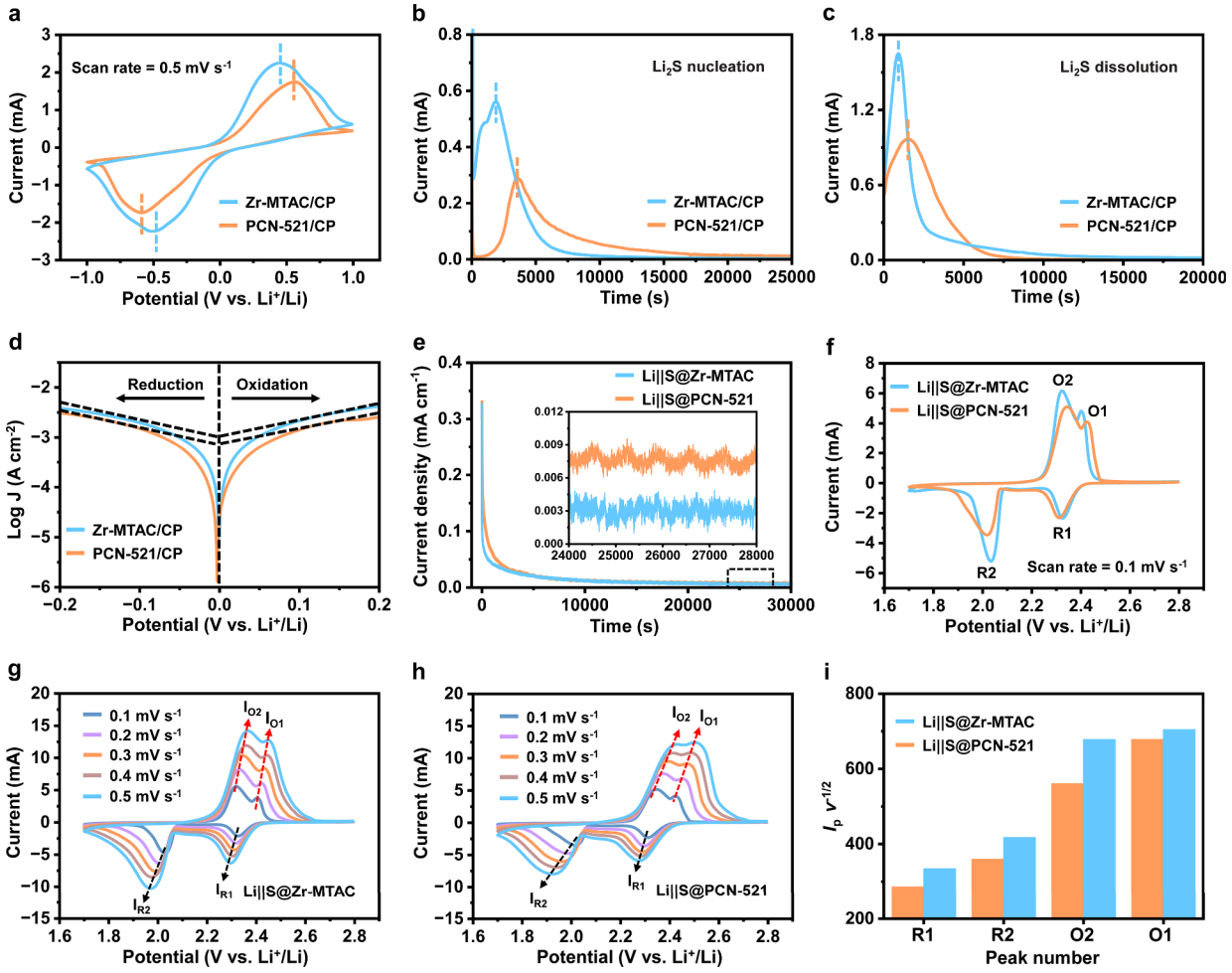

Figure 3. Electrochemical kinetics evaluations for Zr-MTAC and PCN-521 as the host materials of sulfur cathodes. (a) Comparison of CV curves for Li_2S_6 symmetric batteries assembled with Zr-MTAC/CP and PCN-521/CP electrodes at 0.5 mV s^{-1}. (b) Potentiostatic discharge profiles at 2.05 V and (c) charge profiles at 2.35 V for the Zr-MTAC/CP and PCN-521/CP electrodes. (d) Tafel plots of Li_2S_6 symmetric batteries assembled with Zr-MTAC/CP and PCN-521/CP electrodes. (e) Shuttle current density curves of Li||S@Zr-MTAC and Li||S@PCN-521 batteries. The inset shows a partial magnification of the shuttle current density curves. (f) CV curves of Li||S@Zr-MTAC and Li||S@PCN-521 batteries at 0.1 mV s^{-1}. (g, h) CV curves of (g) Li||S@Zr-MTAC and (h) Li||S@PCN-521 batteries at different scan rates from 0.1 to 0.5 mV s^{-1}. (i) Comparison of the linearly fitted slopes obtained by the CV peak currents *vs* the square roots of scan rates ($v^{1/2}$) plots.

the PXRD patterns of fully activated Zr-MTAC, which showed significant peak shifts compared with those of the as-synthesized sample (Figure S8).

The successful construction of Zr-MTAC and PCN-521 was further demonstrated by Fourier transform infrared (FT-IR) spectroscopy. In the FT-IR spectra of the ligands MTAC and MTBC, the strong peak at 1691 cm^{-1} corresponded to C=O stretching in free COOH. For Zr-MTAC and PCN-521, the strong absorption peaks at 1414 and 1410 cm^{-1} originated from the coordinated COO^- groups. Moreover, the appearance of a vibration band at 1459 cm^{-1} was attributed to the N=N stretching vibration, indicating the formation of azo groups in Zr-MTAC (Figure 2b). To collect more evidence about the N=N bonds in the framework structure, Raman spectroscopy analysis was performed. The results of the Raman spectra were consistent with the FT-IR findings, with the appearance of a vibration band at 1459 cm^{-1} attributed to the formation of N=N bonds, further confirming the presence of N=N bonds in the Zr-MTAC structure (Figure 2c). The structure of Zr-MTAC observed by transmission electron microscopy (TEM) matched perfectly with its simulated crystalline models, indicating that the as-synthesized material precisely matches the theoretical framework design (Figure 2d). TEM imaging further provided clear visualization of the long-range crystalline order in Zr-MTAC. The distinct lattice fringes with a lattice spacing of 0.31 nm correspond to the (101) plane (Figure 2e and Figure S9). Scanning electron microscopy (SEM) characterizations revealed that both Zr-MTAC and PCN-521 had a polyhedral morphology with the size in the range of 100−150 μm. The corresponding energy-dispersive X-ray (EDX) elemental mappings confirmed the homogeneous distributions of Zr and N elements for Zr-MTAC and Zr and O elements for PCN-521 (Figure 2f).

To explore the chemical compositions and valence states of the samples, X-ray photoelectron spectroscopy (XPS) measurements were performed (Figure S10a). Four characteristic peaks located at 183.7, 285.1, 399.9, and 531.4 eV were detected in XPS full spectra of Zr-MTAC, corresponding to the Zr 3d, C 1s, N 1s, and O 1s peaks, respectively. The high-resolution XPS spectra of Zr 3d showed two peaks corresponding to Zr $3d_{3/2}$ and Zr $3d_{5/2}$. The higher binding energy at 184.7 eV was assigned to Zr $3d_{3/2}$ of Zr-MTAC and

https://doi.org/10.1021/jacs.5c16469
J. Am. Chem. Soc. XXXX, XXX, XXX−XXX

PCN-521, whereas the peak at 182.3 eV corresponded to Zr $3d_{5/2}$ of Zr-MTAC and PCN-521 (Figure 2g). The high-resolution XPS spectra of O 1s showed three peaks corresponding to three chemical states of oxygen in Zr-MTAC and PCN-521. The three peaks at 529.6 eV (O_L), 531.3 eV (O_V), and 533.1 eV (O_C) were assigned to bridging O^{2-} (Zr−O−Zr), carboxylate oxygen (Zr-COO^-), and hydroxides (Zr−OH), respectively (Figure S10b).[62,63] In the N 1s XPS spectra of Zr-MTAC, two distinct peaks were detected at 402.8 and 400.2 eV, in line with C−N and N=N bonds, respectively, demonstrating the existence of azo groups in the Zr-MTAC structure (Figure 2h). The C 1s XPS spectra of Zr-MTAC could be coherently fitted by three major characteristic peaks, which were assigned to 289.1 eV (O−C=O), 285.6 eV (C−N), and 284.8 eV (C−C/C=C) (Figure 2i). These results collectively demonstrate the successful synthesis of Zr-MTAC and PCN-521 with the desired chemical compositions and functional group architectures.

The PXRD patterns of Zr-MTAC and PCN-521 after immersion in various solvents and aqueous solutions with different pH values (pH = 2, 7, and 12) exhibited well-maintained crystallinity and agreed with the simulated patterns, confirming their superior structural stability (Figure 2j, k). Thermogravimetric analysis (TGA) of Zr-MTAC and PCN-521 showed that both frameworks possessed excellent thermal stability up to 300 °C (Figure S11). Therefore, the melt diffusion method was employed to prepare sulfur-loaded MOF composite materials (denoted as S@Zr-MTAC and S@PCN-521), where sublimed sulfur was introduced into the MOF pores through melting after mechanical mixing with the MOF precursors (Figure S12). Furthermore, TGA measurements confirmed that the sulfur contents of S@Zr-MTAC and S@PCN-521 were 80.3 and 81.6%, respectively, which were basically consistent with the expected 80% sulfur content in the experiments (Figure S13). Additionally, PXRD patterns revealed that the structural integrity of both the Zr-MTAC and PCN-521 MOFs was well maintained after sulfur loading (Figure S14). The intense characteristic peaks of S@Zr-MTAC and S@PCN-521 were primarily attributed to sulfur, illustrating the successful infiltration of sulfur. After sulfur impregnation, the specific surface areas of S@Zr-MTAC and S@PCN-521 composites decreased to 15.12 and 68.40 $m^2\ g^{-1}$, respectively, which further confirmed the successful loading of sulfur in porous Zr-MTAC and PCN-521 (Figure S15). According to the results of FT-IR and Raman spectra, the structures of Zr-MTAC and PCN-521 remained unchanged after sulfur loading, verifying the structural stability of Zr-MTAC and PCN-521 (Figures S16 and S17). EDX elemental mappings revealed the uniform distribution of sulfur in the pores of Zr-MTAC and PCN-521 (Figure S18). The full XPS spectra of the S@Zr-MTAC composite exhibited five characteristic peaks corresponding to S, Zr, C, N, and O. In the S 2p XPS spectra, the characteristic peaks at 163.6 and 162.5 eV were assigned to the S $2p_{1/2}$ and S $2p_{3/2}$ bands of elemental sulfur, respectively. No changes in the chemical compositions or valence states corresponding to the other elements were observed via XPS analysis (Figure S19).

Kinetic Performance of Li−S Batteries. To investigate the electrocatalytic activity of Zr-MTAC and PCN-521 for polysulfide conversion, systematic electrochemical measurements were conducted using Zr-MTAC- or PCN-521-loaded carbon paper electrodes (denoted as Zr-MTAC/CP or PCN-521/CP, respectively). Cyclic voltammetry (CV) measurements of Li_2S_6 symmetric batteries with different carbon paper electrodes were performed at a scan rate of 0.5 mV s^{-1} within the voltage range from −1.0 to 1.0 V (Figure 3a). The Zr-MTAC/CP symmetric batteries displayed a pair of prominent redox peaks at ±0.48 V, corresponding to the reversible redox reactions of Li_2S_6. It suggests that the azo groups in Zr-MTAC/CP act as electron transport channels to accelerate electron transfer. Furthermore, the Zr-MTAC/CP electrodes demonstrated higher electrochemical reactivity in the polysulfide conversion process than PCN-521/CP electrodes at increased scan rates (Figure S20). Electrochemical impedance spectroscopy (EIS) was used to assess the charge-transfer kinetics at the electrode−electrolyte interfaces (Figure S21). The Li_2S_6 symmetric batteries with Zr-MTAC/CP electrodes exhibited a smaller charge-transfer resistance, indicating better mass-transfer kinetics for the Zr-MTAC/CP electrodes.

The nucleation of Li_2S was investigated through the potentiostatic discharge profiles at 2.05 V (Figure 3b). Zr-MTAC/CP electrodes displayed a higher peak current for Li_2S deposition (0.57 mA) compared to those of PCN-521/CP electrodes (0.29 mA). The reduction current response time for Li_2S nucleation on the Zr-MTAC/CP electrodes (1830 s) was much shorter than those on the PCN-521/CP electrodes (3621 s). The dissolution behavior of Li_2S was examined through the potentiostatic charge at 2.35 V (Figure 3c). Zr-MTAC/CP electrodes demonstrated a higher peak current (1.63 mA) and an earlier oxidation current response (935 s) for Li_2S decomposition, indicating highly efficient polysulfide conversion on Zr-MTAC/CP electrodes.[64,65] The above conclusion was verified by measurements of Tafel curves (Figure 3d), which show a higher exchange current density (i_0) for the Zr-MTAC/CP electrodes. Furthermore, shuttle current densities were also measured based on different Li−S batteries. As shown in Figure 3e, the S@Zr-MTAC cathodes exhibited a lower shuttle current relative to the S@PCN-521 cathodes, confirming the effective adsorption of polysulfides and suppression of the shuttle effect.[66]

To demonstrate the polysulfide adsorption effectiveness and electrocatalytic activity of Zr-MTAC as a sulfur host material, the Li−S batteries were assembled using S@Zr-MTAC and S@PCN-521 cathodes. The CV curves of Li||S@Zr-MTAC and Li||S@PCN-521 batteries were recorded for the first three cycles within the voltage window of 1.7−2.8 V at a scan rate of 0.1 mV s^{-1}. As shown in Figure S22, the CV curves of two-type Li−S batteries exhibited two pairs of sharp redox peaks, corresponding to multistep electrochemical redox processes of sulfur cathodes. Notably, the CV curves of the Li||S@Zr-MTAC batteries exhibited a smaller voltage difference of redox peaks (Figure 3f), and peak current densities were higher than those of Li||S@PCN-521 batteries, indicating superior electrocatalytic activity and improved polysulfide redox kinetics of S@Zr-MTAC cathodes. The CV curves of Li||S@Zr-MTAC and Li||S@PCN-521 batteries were also measured at various scan rates ranging from 0.1 to 0.5 mV s^{-1} (Figure 3g, h). With the increase of scan rates, both of the Li−S batteries exhibited gradually increasing current responses, but the Li||S@Zr-MTAC batteries demonstrated higher redox peak currents and lower polarization potentials compared with the Li||S@PCN-521 batteries. By linear fitting of CV peak currents with the square root of scan rates, the Li^+ diffusion coefficients (D_{Li}^+) of different Li−S batteries were calculated based on the classical Randles−Sevcik equation.[67] The fitting results confirmed that the Li||S@Zr-MTAC batteries exhibited sharper slopes (Figure

https://doi.org/10.1021/jacs.5c16469
J. Am. Chem. Soc. XXXX, XXX, XXX−XXX

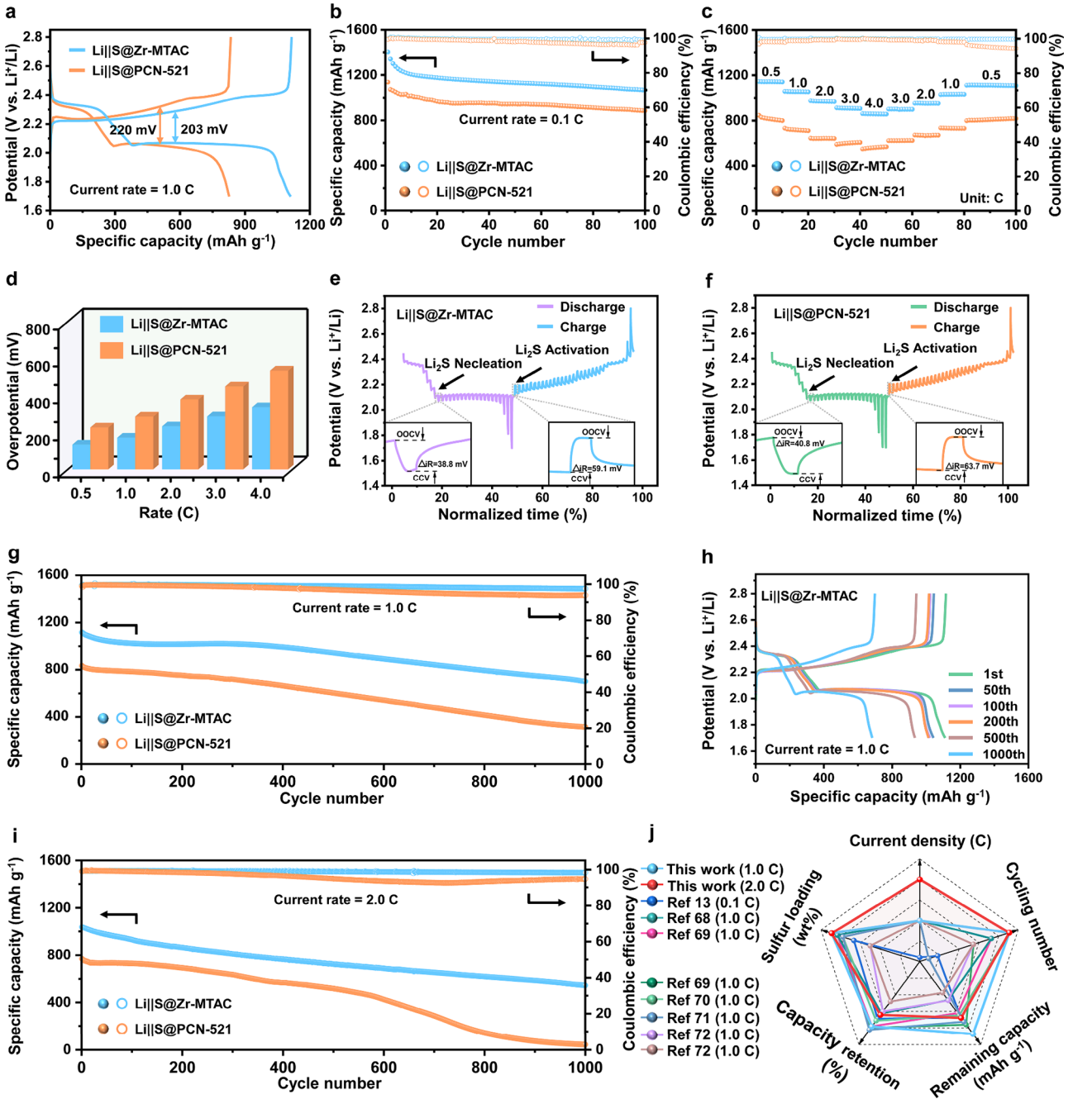

Figure 4. Electrochemical performances of Li−S batteries based on the S@Zr-MTAC and S@PCN-521 cathodes. (a) Comparison of galvanostatic charge−discharge profiles of Li||S@Zr-MTAC and Li||S@PCN-521 batteries at 1.0 C. (b) Cycling performances of Li||S@Zr-MTAC and Li||S@PCN-521 batteries at 0.1 C. (c) Rate performances of Li||S@Zr-MTAC and Li||S@PCN-521 batteries at various current rates from 0.5 to 4.0 C. (d) Potential differences between the charge/discharge plateaus of Li||S@Zr-MTAC and Li||S@PCN-521 batteries. (e, f) Galvanostatic intermittent titration technique profiles of (e) Li||S@Zr-MTAC and (f) Li||S@PCN-521 batteries. (g) Cycling performances of Li||S@Zr-MTAC and Li||S@PCN-521 batteries at 1.0 C. (h) Galvanostatic charge/discharge profiles during different cycles for Li||S@Zr-MTAC batteries at 1.0 C. (i) Cycling performances of Li||S@Zr-MTAC and Li||S@PCN-521 batteries at 2.0 C. (j) Comparison of the electrochemical performances of Li||S@Zr-MTAC batteries with previously reported Li−S batteries based on different MOF/COF host materials.

3i and Figure S23), indicating more rapid Li^+ diffusion during the redox reactions. Specifically, for reduction peaks (I_{R1}, I_{R2}) and oxidation peaks (I_{O2}, I_{O1}), the Li||S@Zr-MTAC batteries were characterized by D_{Li^+} values of 5.23×10^{-6}, 3.02×10^{-7}, 2.15×10^{-5}, and 8.60×10^{-7} cm^2 s^{-1}, respectively, much higher than those of Li||S@PCN-521 batteries (Table S3). The faster Li^+ conducting behavior was attributed to the suppression of the shuttling effect and the electrocatalytic activity of the Zr-MTAC host, enabled by its azo-functionalized active sites for accelerating polysulfide conversion kinetics. These properties contributed to preventing the formation of a high-viscosity electrolyte environment caused by both the dissolution of polysulfides and the deposition of insulating Li_2S_2/Li_2S on electrodes.[43,67]

To verify that the framework material maintains structural stability during the cycling of Li−S batteries, we conducted

https://doi.org/10.1021/jacs.5c16469
J. Am. Chem. Soc. XXXX, XXX, XXX−XXX

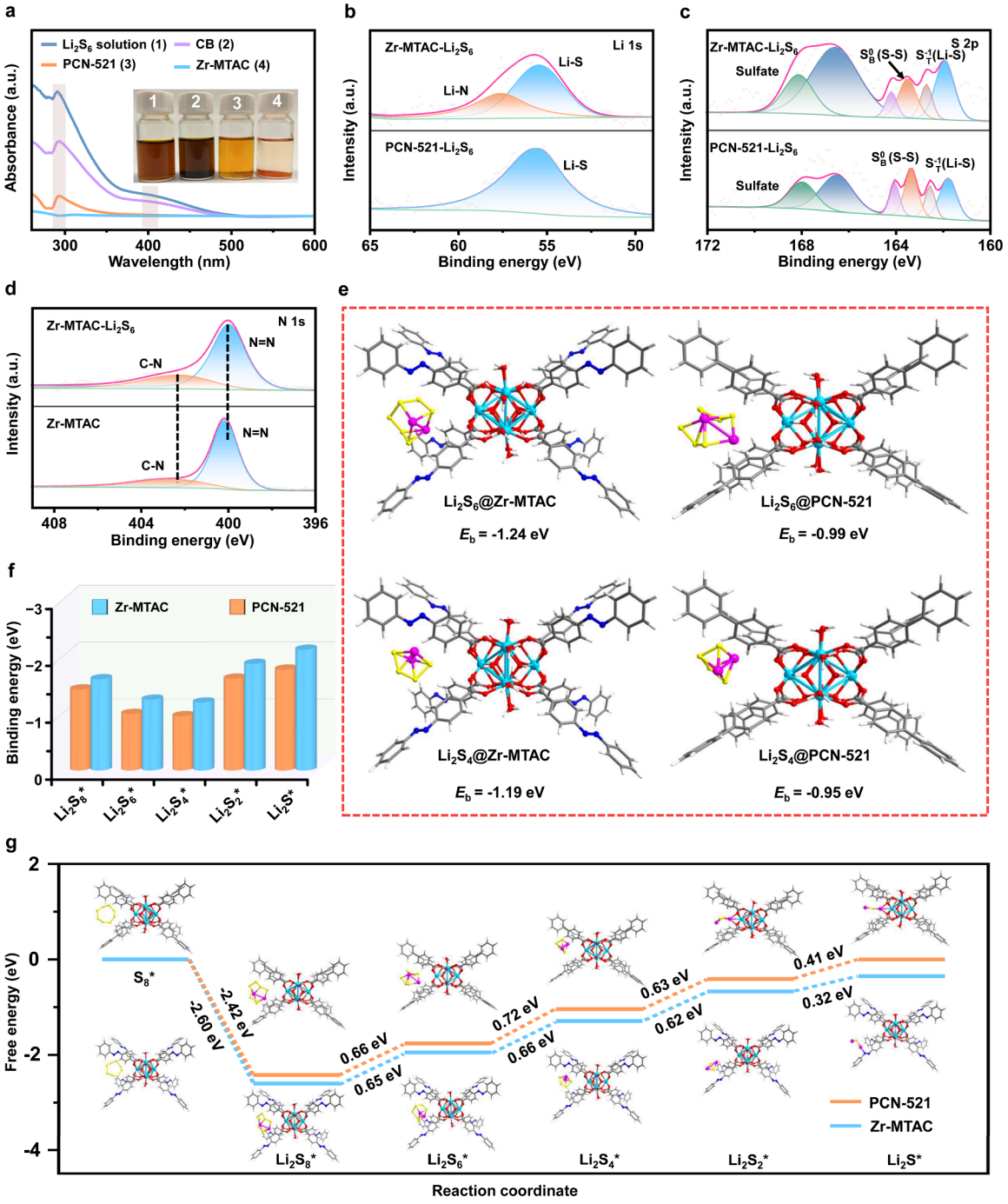

Figure 5. Chemical adsorption behaviors and DFT-calculated reaction pathways of Zr-MTAC and PCN-521 for polysulfide conversion. (a) UV–vis absorption spectra and (the inset) optical images of a pristine Li_2S_6 solution and Li_2S_6 solutions mixed with Zr-MTAC, PCN-521, and CB host materials. (b, c) High-resolution XPS spectra at (b) Li 1s and (c) S 2p regions of Zr-MTAC and PCN-521 after the adsorption of Li_2S_6 solution. (d) High-resolution XPS spectra at the N 1s level of Zr-MTAC before and after the adsorption of Li_2S_6 solution. (e) Optimized geometric configurations and binding energies of Li_2S_6 and Li_2S_4 absorbed on Zr-MTAC and PCN-521 models. (f) Binding free energies between LiPSs adsorbed on Zr-MTAC and PCN-521 units were calculated by DFT. (g) Calculated Gibbs free energies for the stepwise reduction of S_x^{2-} species on the Zr-MTAC and PCN-521 units.

Raman and XRD spectroscopic characterizations of the composite sulfur cathodes after cycling. Raman spectroscopy analysis on the desulfurized Zr-MTAC electrodes clearly showed that the characteristic stretching vibration of azo groups at 1459 cm^{-1} remained intact before and after charge/discharge cycles (Figure S24). Moreover, the PXRD patterns of Zr-MTAC and PCN-521 confirmed that the crystal structures of MOFs remained identical after charge/discharge cycles (Figure S25).

Cycling Performances of Li–S Batteries. The galvanostatic charge/discharge behaviors of the Li–S batteries based on S@Zr-MTAC and S@PCN-521 cathodes were investigated at a current rate of 1.0 C. As displayed in Figure 4a, the LillS@Zr-MTAC batteries exhibited a lower potential hysteresis and higher discharge capacity than LillS@PCN-521 batteries,

https://doi.org/10.1021/jacs.5c16469
J. Am. Chem. Soc. XXXX, XXX, XXX–XXX

indicating improved electrode polarization and accelerated reaction kinetics. Figure 4b shows the cycling performances of LillS@Zr-MTAC and LillS@PCN-521 batteries. After 100 cycles at 0.1 C, the reversible discharge capacity of the batteries with S@Zr-MTAC cathodes remained at 1065.6 mAh g^{-1}, suggesting that the S@Zr-MTAC cathodes can effectively block the shuttle effect of polysulfides, while the capacity of the batteries with S@PCN-521 cathodes retained only 884.5 mAh g^{-1}. The rate performances of LillS@Zr-MTAC and LillS@PCN-521 batteries were tested by cycling at various current rates ranging from 0.5 to 4.0 C (Figure 4c). The LillS@Zr-MTAC batteries delivered specific discharge capacities of 1139.8, 1052.9, 967.1, 906.2, and 856.5 mAh g^{-1} at 0.5, 1.0, 2.0, 3.0, and 4.0 C, respectively. When the current rate returned to 0.5 C, a well-recovered discharge capacity of 1107.5 mAh g^{-1} was obtained, suggesting superior rate performance and electrochemical stability for the S@Zr-MTAC cathodes. The superior rate performance of S@Zr-MTAC cathodes should be attributed to the lower polarization and better reaction kinetics than S@PCN-521 cathodes, which was confirmed by the smaller potential differences between the charge/discharge plateaus of S@Zr-MTAC cathodes (Figure 4d and Figure S26).

EIS analyses of the LillS@Zr-MTAC and LillS@PCN-521 batteries were conducted to verify the accelerated charge-transfer kinetics (Figure S27). Before cycling (Figure S27a), the LillS@Zr-MTAC batteries had a lower charge-transfer resistance (21.7 Ω) than the LillS@PCN-521 batteries (38.8 Ω). After 50 cycles, the charge-transfer resistance corresponding to the LillS@Zr-MTAC batteries further decreased to 3.1 Ω, which is much lower than those of the LillS@PCN-521 batteries (19.3 Ω) (Figure S27b), demonstrating faster polysulfide conversion kinetics for the S@Zr-MTAC cathodes. By further conducting EIS analyses after different cycles, the charge-transfer resistances of the LillS@Zr-MTAC batteries were well maintained during the extended cycling process, while those of the LillS@PCN-521 batteries initially decreased and then increased as the cycling process progressed, demonstrating the formation of more stable interfaces in the LillS@Zr-MTAC batteries to support rapid ion-transport kinetics throughout cycling (Figure S27c,d and Tables S4 and S5). The galvanostatic intermittent titration technique (GITT) was further employed to investigate the real-time internal resistances, as shown in Figure 4e, f. The LillS@Zr-MTAC batteries exhibited lower internal resistances at the nucleation points of Li_2S and the activation points of Li_2S dissolution (inset in Figure 4e) than the LillS@PCN-521 batteries, indicating a lower energy barrier for the sulfur redox reactions. The long-term cycling stabilities of Li−S batteries with the S@Zr-MTAC and S@PCN-521 cathodes were evaluated at current rates of 0.5 1.0, and 2.0 C. After 500 cycles at 0.5 C, the LillS@Zr-MTAC batteries still delivered a discharge capacity of 889.1 mAh g^{-1} and a stable Coulombic efficiency of over 98.5%, while the LillS@PCN-521 batteries exhibited a discharge capacity of 563.1 mAh g^{-1} and a Coulombic efficiency of only 93.6%. The LillS@Zr-MTAC batteries demonstrated well-defined galvanostatic charge/discharge profiles with low voltage polarization across various cycles (Figure S28). When cycled at a current rate of 1.0 C (Figure 4g), the LillS@Zr-MTAC batteries exhibited an initial discharge capacity of 1115.6 mAh g^{-1} and a considerable remaining capacity of 699.4 mAh g^{-1} over 1000 cycles, corresponding to a capacity decay ratio of only 0.037% per cycle. In contrast, the LillS@PCN-521 batteries suffered from fast capacity loss, with a large capacity decay ratio of 0.062% per cycle. The LillS@Zr-MTAC batteries exhibited well-shaped galvanostatic charge/discharge profiles with low voltage polarization at different cycles, while LillS@PCN-521 batteries showed significant voltage hysteresis, poor cycling reversibility, and rapid capacity attenuation (Figure 4h and Figure S29). The above results indicated that the LillS@Zr-MTAC batteries achieved a significantly enhanced cycling performance. Even at a higher current density of 2.0 C (Figure 4i), the LillS@Zr-MTAC batteries could still deliver a reversible discharge capacity of 543.3 mAh g^{-1} and a high Coulombic efficiency of 98.0% after 1000 cycles, which were significantly higher than those of LillS@PCN-521 batteries (43.4 mAh g^{-1} and 94.0%). The absence of azo groups in PCN-521 leads to weaker polysulfide affinity and slower conversion kinetics, rendering it more susceptible to shuttle effects during high-rate cycling. Notably, when compared with previously reported MOF or covalent organic framework (COF) based host materials applied in Li−S batteries, the S@Zr-MTAC cathodes delivered highly competitive specific capacity and cycling stability, as presented in Figure 4j and Table S6.[13,68−72]

The high areal S loading is essential for fabricating practical high-energy-density Li−S batteries. As shown in Figure S30, the LillS@Zr-MTAC batteries with an areal sulfur loading of 3.0 mg cm^{-2} delivered an initial discharge capacity of 3.5 mAh cm^{-2} at 0.2 C and a capacity retention of 83.4% after 120 cycles. When the areal sulfur loading was increased to 5.0 mg cm^{-2}, the initial discharge capacity was raised to 4.9 mAh cm^{-2}, and a considerable discharge capacity of 4.0 mAh cm^{-2} was provided after 120 cycles. Even with an ultrahigh sulfur loading of 6.5 mg cm^{-2}, the LillS@Zr-MTAC batteries still exhibited an appreciable initial areal capacity as high as 5.8 mAh cm^{-2} and retained a capacity of 4.6 mAh cm^{-2} (corresponding to a capacity retention of 79.3%) after 120 cycles. These results highlighted the excellent cycling stability and reversibility of S@Zr-MTAC cathodes, demonstrating their great application potential for practical Li−S batteries.

Theoretical Prediction of Accelerated Polysulfide Conversion by Zr-MTAC and PCN-521 Hosts. To investigate the chemical adsorption of polysulfides by Zr-MTAC, PCN-521, and conventional carbon blank (CB) host materials, the parallel adsorption experiments of Li_2S_6 solutions were carried out and the adsorption degrees were checked by ultraviolet−visible (UV−vis) spectroscopy (Figure 5a). After 12 h, nearly colorless solutions were obtained with Zr-MTAC, demonstrating its prominent chemical adsorption capacity for polysulfides compared with PCN-521 and CB. This observation was further confirmed by the results of the UV−vis adsorption spectra. The characteristic peaks within the range of 280−300 nm corresponded to the presence of Li_2S_6, while the broad absorption peak observed at approximately 400 nm was attributed to Li_2S_4.[73−75] The Zr-MTAC showed the lowest absorbance intensity, indicating the strongest chemical adsorption ability toward polysulfides. As shown in Figure S31, PXRD analyses revealed that the characteristic diffraction peaks of both Zr-MTAC and PCN-521 samples were well retained after immersion in polysulfide solution, confirming the intact preservation of their crystalline frameworks. Furthermore, the superior capture ability of the Zr-MTAC host material for polysulfides was confirmed by XPS analysis. After the Li_2S_6 adsorption, the Li 1s XPS spectra (Figure 5b) of the Zr-MTAC-Li_2S_6 and PCN-521-Li_2S_6 mixtures exhibited a

https://doi.org/10.1021/jacs.5c16469
J. Am. Chem. Soc. XXXX, XXX, XXX−XXX

characteristic peak at 55.47 eV, corresponding to the Li−S bond in Li_2S_6, while the Zr-MTAC-Li_2S_6 mixture showed an additional peak at 57.58 eV corresponding to the Li−N bond.[76] Moreover, the pristine Li_2S_6 sample exhibited two peaks located at 161.7 and 163.3 eV, corresponding to the terminal (S_T^{-1}) and bridging (S_B^0) sulfur atoms, respectively.[77] As shown in Figure 5c, all S 2p bands were deconvoluted into two subpeaks by spin−orbit splitting (S $2p_{1/2}$ and S $2p_{3/2}$).[78,79] Specifically, the peaks associated with S_T^{-1} and S_B^0 atoms in the S 2p XPS spectrum of Zr-MTAC-Li_2S_6 were observed at 161.9 and 163.5 eV, respectively. The significant positive binding energy shift in the S 2p XPS spectrum of the Zr-MTAC-Li_2S_6 mixture confirmed the strong chemical interaction between Li_2S_6 and Zr-MTAC. However, in the S 2p XPS spectrum of the PCN-521-Li_2S_6 system, no binding energy shift was observed for the two peaks. Meanwhile, the N 1s XPS spectrum of the Zr-MTAC-Li_2S_6 mixture (Figure 5d) showed that the chemical adsorption of polysulfides by azo groups increased the electron cloud density of nitrogen atoms, leading to a decrease in binding energy and an obvious negative binding energy shift. The positive binding energy shift in the S 2p XPS spectrum and the negative binding energy shift in the N 1s XPS spectrum affirmatively supported the strong chemical interaction between Zr-MTAC and Li_2S_6. Taking the Li_2S_6-adsorbed and Li_2S_4-adsorbed structures as examples (Figure 5e), the calculated binding energies (E_b) were −1.24 and −1.19 eV for Zr-MTAC and −0.99 and −0.95 eV for PCN-521, respectively. Figure 5f further displays the E_b of lithium polysulfide (LiPSs) species at five different lithiation stages. DFT calculations revealed that Zr-MTAC exhibited significantly higher absolute binding energies than PCN-521. These results demonstrated strong chemisorption of LiPSs species on Zr-MTAC, attributed to the azo groups within the framework, indicating its high potential for suppressing the polysulfide shuttle effect.

DFT calculations were further performed to explore the sulfur reduction pathways in the Zr-MTAC and PCN-521 hosts, as shown in Figure 5g. The reversible formation of Li_2S from S_8 and Li was investigated, and the optimized structures of intermediates on both substrates are shown in Figures S32 and S33. In this process, the first step involved the double reduction of S_8 with two Li^+ ions to form Li_2S_8, and then Li_2S_8 underwent further reduction to form three intermediate polysulfides (Li_2S_6, Li_2S_4, and Li_2S_2) to ultimately produce Li_2S as the final product. The solid−solid conversion from Li_2S_2 to Li_2S was regarded as the rate-determining step because of the sluggish kinetics of this electrochemical conversion.[68,80] The free energy increase for Zr-MTAC was lower than that for PCN-521, suggesting that the reduction of sulfur species was more thermodynamically favorable for Zr-MTAC compared to PCN-521. The synergistic effect of azo groups and Zr-oxo clusters promoted the electrocatalytic conversion of polysulfides and reduced the activation energy of the reaction. Within the operational voltage window of Li−S batteries, the azo groups in Zr-MTAC remained electrochemically inactive, as evidenced by the absence of characteristic lithiation/delithiation redox peaks, confirming their noninvolvement in the lithium storage mechanism (Figure S34). The introduction of azo groups, which serve as electron transport channels to accelerate electron transfer (Figure S35), significantly enhanced the electrocatalytic activity and showed great potential as effective host materials for promoting Li−S redox reactions.

CONCLUSIONS

In summary, we report the structural design and synthesis of an azo-functionalized MOF, Zr-MTAC, which can serve as an efficient cathodic host material in Li−S batteries. The incorporated azo groups not only enable effective capture of polysulfides but also function as electron transport channels to accelerate the nucleation/dissolution of solid-state Li_2S. The synergistic effect of azo groups and Zr-oxo clusters has been proven to reduce the reaction energy barrier on the cathodic side and promote the catalytic conversion of polysulfides. Consequently, the S@Zr-MTAC cathode exhibits a high reversible specific capacity of 1115.6 mAh g^{-1} and superior cycling stability for 1000 cycles at 1.0 C, with a capacity decay rate of only 0.037% per cycle. Additionally, an exceptional rate capability is achieved for the S@Zr-MTAC cathode, retaining 856.5 mAh g^{-1} at a high current rate of 4.0 C. This work presents a promising coordination architecture design strategy for MOF host materials in Li−S batteries, effectively demonstrating their application potential and paving the way for the utilization of azo-functionalized MOFs in energy storage systems.

ASSOCIATED CONTENT

Supporting Information

The Supporting Information is available free of charge at https://pubs.acs.org/doi/10.1021/jacs.5c16469.

Materials and instrumentation, detailed experimental procedures, characterization analysis, and electrochemical measurement, including Figures S1−S35 and Tables S1−S6 (PDF)

Accession Codes

Deposition Number 2486673 contains the supplementary crystallographic data for this paper. These data can be obtained free of charge via the joint Cambridge Crystallographic Data Centre (CCDC) and Fachinformationszentrum Karlsruhe Access Structures service.

AUTHOR INFORMATION

Corresponding Authors

Pei-Chen Zhao − *State Key Laboratory of Coordination Chemistry, MOE Key Laboratory of Mesoscopic Chemistry, MOE Key Laboratory of High Performance Polymer Materials and Technology, Jiangsu Key Laboratory of Advanced Organic Materials, Suzhou Key Laboratory of Green Intelligent Manufacturing of New Energy Materials and Devices, Tianchang New Materials and Energy Technologies Research Center, Institute of Green Chemistry and Engineering, School of Chemistry and Chemical Engineering, Nanjing University, Nanjing, Jiangsu 210023, P. R. China;* orcid.org/0000-0003-2847-1587; Email: lemon_zhao@nju.edu.cn

Shuai Yuan − *State Key Laboratory of Coordination Chemistry, MOE Key Laboratory of Mesoscopic Chemistry, MOE Key Laboratory of High Performance Polymer Materials and Technology, Jiangsu Key Laboratory of Advanced Organic Materials, Suzhou Key Laboratory of Green Intelligent Manufacturing of New Energy Materials and Devices, Tianchang New Materials and Energy Technologies Research Center, Institute of Green Chemistry and Engineering, School of Chemistry and Chemical Engineering, Nanjing University, Nanjing, Jiangsu 210023, P.*

https://doi.org/10.1021/jacs.5c16469
J. Am. Chem. Soc. XXXX, XXX, XXX−XXX

R. China; orcid.org/0000-0003-3329-0481; Email: syuan@nju.edu.cn

Zhong Jin − *State Key Laboratory of Coordination Chemistry, MOE Key Laboratory of Mesoscopic Chemistry, MOE Key Laboratory of High Performance Polymer Materials and Technology, Jiangsu Key Laboratory of Advanced Organic Materials, Suzhou Key Laboratory of Green Intelligent Manufacturing of New Energy Materials and Devices, Tianchang New Materials and Energy Technologies Research Center, Institute of Green Chemistry and Engineering, School of Chemistry and Chemical Engineering, Nanjing University, Nanjing, Jiangsu 210023, P. R. China*; orcid.org/0000-0001-8860-8579; Email: zhongjin@nju.edu.cn

Cheng-Hui Li − *State Key Laboratory of Coordination Chemistry, MOE Key Laboratory of Mesoscopic Chemistry, MOE Key Laboratory of High Performance Polymer Materials and Technology, Jiangsu Key Laboratory of Advanced Organic Materials, Suzhou Key Laboratory of Green Intelligent Manufacturing of New Energy Materials and Devices, Tianchang New Materials and Energy Technologies Research Center, Institute of Green Chemistry and Engineering, School of Chemistry and Chemical Engineering, Nanjing University, Nanjing, Jiangsu 210023, P. R. China*; orcid.org/0000-0001-8982-5938; Email: chli@nju.edu.cn

Authors

Wei Meng − *State Key Laboratory of Coordination Chemistry, MOE Key Laboratory of Mesoscopic Chemistry, MOE Key Laboratory of High Performance Polymer Materials and Technology, Jiangsu Key Laboratory of Advanced Organic Materials, Suzhou Key Laboratory of Green Intelligent Manufacturing of New Energy Materials and Devices, Tianchang New Materials and Energy Technologies Research Center, Institute of Green Chemistry and Engineering, School of Chemistry and Chemical Engineering, Nanjing University, Nanjing, Jiangsu 210023, P. R. China*

Yaoda Wang − *State Key Laboratory of Coordination Chemistry, MOE Key Laboratory of Mesoscopic Chemistry, MOE Key Laboratory of High Performance Polymer Materials and Technology, Jiangsu Key Laboratory of Advanced Organic Materials, Suzhou Key Laboratory of Green Intelligent Manufacturing of New Energy Materials and Devices, Tianchang New Materials and Energy Technologies Research Center, Institute of Green Chemistry and Engineering, School of Chemistry and Chemical Engineering, Nanjing University, Nanjing, Jiangsu 210023, P. R. China*

Xiaocheng Zhou − *State Key Laboratory of Coordination Chemistry, MOE Key Laboratory of Mesoscopic Chemistry, MOE Key Laboratory of High Performance Polymer Materials and Technology, Jiangsu Key Laboratory of Advanced Organic Materials, Suzhou Key Laboratory of Green Intelligent Manufacturing of New Energy Materials and Devices, Tianchang New Materials and Energy Technologies Research Center, Institute of Green Chemistry and Engineering, School of Chemistry and Chemical Engineering, Nanjing University, Nanjing, Jiangsu 210023, P. R. China*

Zong-Ju Chen − *State Key Laboratory of Coordination Chemistry, MOE Key Laboratory of Mesoscopic Chemistry, MOE Key Laboratory of High Performance Polymer Materials and Technology, Jiangsu Key Laboratory of Advanced Organic Materials, Suzhou Key Laboratory of Green Intelligent Manufacturing of New Energy Materials and Devices, Tianchang New Materials and Energy Technologies Research Center, Institute of Green Chemistry and Engineering, School of Chemistry and Chemical Engineering, Nanjing University, Nanjing, Jiangsu 210023, P. R. China*

Yue Zhao − *State Key Laboratory of Coordination Chemistry, MOE Key Laboratory of Mesoscopic Chemistry, MOE Key Laboratory of High Performance Polymer Materials and Technology, Jiangsu Key Laboratory of Advanced Organic Materials, Suzhou Key Laboratory of Green Intelligent Manufacturing of New Energy Materials and Devices, Tianchang New Materials and Energy Technologies Research Center, Institute of Green Chemistry and Engineering, School of Chemistry and Chemical Engineering, Nanjing University, Nanjing, Jiangsu 210023, P. R. China*; orcid.org/0000-0001-6094-4087

Complete contact information is available at: https://pubs.acs.org/10.1021/jacs.5c16469

Author Contributions

#W. M. and Y. W. contributed equally to this work.

Notes

The authors declare no competing financial interest.

■ ACKNOWLEDGMENTS

The authors appreciate the financial support from the National Natural Science Foundation of China (22425106, 22271139, 22271141, 22479074, and 22475096), the Fundamental Research Funds for the Central Universities (020514380294 and 2024300376), the National Key Research and Development Program of China (no. 2024YFA1510301), the Equipment Pre-Research and Ministry of Education Joint Fund General Project (no. 8091B02052407), the Natural Science Foundation of Jiangsu Province (nos. BK20240400 and BK20241236), the Jiangsu Province Science and Technology Major Project (no. BG2024013), the Jiangsu Province Scientific and Technological Achievements Transformation Special Fund (no. BA2023037), the Jiangsu Province Academic Degree and Postgraduate Education Reform Project (no. JGKT24_C001), the Suzhou City Key Core Technology Open Competition Project (no. SYG2024122), the Open Research Fund of Suzhou Laboratory (no. SZLAB-1308-2024-TS005), the Suzhou City Gusu Leading Talent Program of Scientific and Technological Innovation and Entrepreneurship in Wujiang District (no. ZXL2021273), and the Chenzhou National Sustainable Development Agenda Innovation Demonstration Zone Provincial Special Project (no. 2023sfq11).

■ REFERENCES

(1) Seh, Z. W.; Sun, Y.; Zhang, Q.; Cui, Y. Designing high-energy lithium−sulfur batteries. *Chem. Soc. Rev.* **2016**, *45* (20), 5605−5634.

(2) Winter, M.; Barnett, B.; Xu, K. Before Li Ion Batteries. *Chem. Rev.* **2018**, *118* (23), 11433−11456.

(3) Kim, J.; Kim, Y.; Yoo, J.; Kwon, G.; Ko, Y.; Kang, K. Organic batteries for a greener rechargeable world. *Nat. Rev. Mater.* **2023**, *8* (1), 54−70.

(4) Chen, Z.; Pan, J.; Huang, W.; Shi, K.; Yang, Z.; Wu, H.; Wei, S.; Jiang, G.; Zou, W.; Zhang, R.; Li, X.; Liu, Q. Heterogeneity-Segment Charge-Induced-Coupling Catalysis of Component-Selective-Type Covalent Organic Frameworks Interface toward Stabilizing Lithium Metal Anode. *ACS Nano* **2025**, *19* (13), 13160−13174.

(5) Sathiya, M.; Rousse, G.; Ramesha, K.; Laisa, C. P.; Vezin, H.; Sougrati, M. T.; Doublet, M. L.; Foix, D.; Gonbeau, D.; Walker, W.; Prakash, A. S.; Ben Hassine, M.; Dupont, L.; Tarascon, J. M. Reversible anionic redox chemistry in high-capacity layered-oxide electrodes. *Nat. Mater.* **2013**, *12* (9), 827−835.
(6) Jiang, Q.; Xiong, P.; Liu, J.; Xie, Z.; Wang, Q.; Yang, X.-Q.; Hu, E.; Cao, Y.; Sun, J.; Xu, Y.; Chen, L. A Redox-Active 2D Metal-Organic Framework for Efficient Lithium Storage with Extraordinary High Capacity. *Angew. Chem., Int. Ed.* **2020**, *59* (13), 5273−5277.
(7) Qi, F.; Sun, Z.; Fan, X.; Wang, Z.; Shi, Y.; Hu, G.; Li, F. Tunable Interaction between Metal−Organic Frameworks and Electroactive Components in Lithium−Sulfur Batteries: Status and Perspectives. *Adv. Energy Mater.* **2021**, *11* (20), 2100387.
(8) Chen, Y.; Wang, T.; Tian, H.; Su, D.; Zhang, Q.; Wang, G. Advances in Lithium-Sulfur Batteries: From Academic Research to Commercial Viability. *Adv. Mater.* **2021**, *33* (29), 2003666.
(9) Li, G.; Lei, W.; Luo, D.; Deng, Y.; Wang, D.; Chen, Z. 3D Porous Carbon Sheets with Multidirectional Ion Pathways for Fast and Durable Lithium-Sulfur Batteries. *Adv. Energy Mater.* **2017**, *8* (8), 1702381.
(10) Peng, H.-J.; Huang, J.-Q.; Liu, X.-Y.; Cheng, X.-B.; Xu, W.-T.; Zhao, C.-Z.; Wei, F.; Zhang, Q. Healing High-Loading Sulfur Electrodes with Unprecedented Long Cycling Life: Spatial Heterogeneity Control. *J. Am. Chem. Soc.* **2017**, *139* (25), 8458−8466.
(11) Li, W.; Guo, X.; Geng, P.; Du, M.; Jing, Q.; Chen, X.; Zhang, G.; Li, H.; Xu, Q.; Braunstein, P.; Pang, H. Rational Design and General Synthesis of Multimetallic Metal-Organic Framework Nano−Octahedra for Enhanced Li−S Battery. *Adv. Mater.* **2021**, *33* (45), 2105163.
(12) Zhu, Z.; Zeng, Y.; Pei, Z.; Luan, D.; Wang, X.; Lou, X. W. Bimetal-Organic Framework Nanoboxes Enable Accelerated Redox Kinetics and Polysulfide Trapping for Lithium-Sulfur Batteries. *Angew. Chem., Int. Ed.* **2023**, *62* (31), No. e202305828.
(13) Geng, P.; Du, M.; Guo, X.; Pang, H.; Tian, Z.; Braunstein, P.; Xu, Q. Bimetallic Metal-Organic Framework with High-Adsorption Capacity toward Lithium Polysulfides for Lithium−sulfur Batteries. *Energy Environ. Mater.* **2022**, *5* (2), 599−607.
(14) Jarrín, R. A.; Bennett, K.; Thoi, V. S.; Bukowski, B. C. Cations Mediate Lithium Polysulfide Adsorption in Metal-Organic Frameworks for Lithium-Sulfur Batteries. *J. Phys. Chem. C* **2023**, *127* (43), 21431−21439.
(15) Zhou, X.; Wang, Y.; Gu, Y.; Su, J.; Liu, Y.; Yin, Y.; Yuan, S.; Ma, J.; Jin, Z.; Zuo, J.-L. All-purpose redox-active metal−organic frameworks as both cathodic and anodic host materials for advanced lithium-sulfur batteries. *Matter* **2024**, *7* (9), 3069−3082.
(16) Cha, E.; Patel, M. D.; Park, J.; Hwang, J.; Prasad, V.; Cho, K.; Choi, W. 2D MoS_2 as an efficient protective layer for lithium metal anodes in high-performance Li−S batteries. *Nat. Nanotechnol.* **2018**, *13* (4), 337−344.
(17) Wang, W.; Yue, X.; Meng, J.; Wang, J.; Wang, X.; Chen, H.; Shi, D.; Fu, J.; Zhou, Y.; Chen, J.; Fu, Z. Lithium phosphorus oxynitride as an efficient protective layer on lithium metal anodes for advanced lithium−sulfur batteries. *Energy Storage Mater.* **2019**, *18*, 414−422.
(18) Al Salem, H.; Babu, G.; V. Rao, C.; Arava, L. M. R. Electrocatalytic Polysulfide Traps for Controlling Redox Shuttle Process of Li−S Batteries. *J. Am. Chem. Soc.* **2015**, *137* (36), 11542−11545.
(19) Jiao, L.; Zhang, C.; Geng, C.; Wu, S.; Li, H.; Lv, W.; Tao, Y.; Chen, Z.; Zhou, G.; Li, J.; Ling, G.; Wan, Y.; Yang, Q. Capture and Catalytic Conversion of Polysulfides by In Situ Built TiO_2−MXene Heterostructures for Lithium-Sulfur Batteries. *Adv. Energy Mater.* **2019**, *9* (19), 1900219.
(20) Meng, R.; Du, Q.; Zhong, N.; Zhou, X.; Liu, S.; Yin, S.; Liang, X. A Tandem Electrocatalysis of Sulfur Reduction by Bimetal 2D MOFs. *Adv. Energy Mater.* **2021**, *11* (47), 2102819.
(21) Ren, X.; Wang, Q.; Pu, Y.; Sun, Q.; Sun, W.; Lu, L. Synergizing Spatial Confinement and Dual-Metal Catalysis to Boost Sulfur Kinetics in Lithium-Sulfur Batteries. *Adv. Mater.* **2023**, *35* (44), 2304120.
(22) Liu, Q.; Wu, Y.; Li, D.; Peng, Y.; Liu, X.; Li, B.; Huang, J.; Peng, H. Dilute Alloying to Implant Activation Centers in Nitride Electrocatalysts for Lithium-Sulfur Batteries. *Adv. Mater.* **2022**, *35* (7), 2209233.
(23) Liang, F.; Xiang, H.; Guo, M.; Liu, X.; Zhu, J. Lewis Acidic/Basic Oxides Modulated Cu_3P for Efficient Lithium Polysulfide Electrocatalytic Conversion. *Adv. Funct. Mater.* **2025**, No. e12654.
(24) Li, H.; Eddaoudi, M.; O'Keeffe, M.; Yaghi, O. M. Design and synthesis of an exceptionally stable and highly porous metalorganic framework. *Nature* **1999**, *402*, 276−279.
(25) Xu, W.; Pei, X.; Diercks, C. S.; Lyu, H.; Ji, Z.; Yaghi, O. M. A Metal-Organic Framework of Organic Vertices and Polyoxometalate Linkers as a Solid-State Electrolyte. *J. Am. Chem. Soc.* **2019**, *141* (44), 17522−17526.
(26) Yuan, S.; Feng, L.; Wang, K.; Pang, J.; Bosch, M.; Lollar, C.; Sun, Y.; Qin, J.; Yang, X.; Zhang, P.; Wang, Q.; Zou, L.; Zhang, Y.; Zhang, L.; Fang, Y.; Li, J.; Zhou, H. Stable Metal-Organic Frameworks: Design, Synthesis, and Applications. *Adv. Mater.* **2018**, *30* (37), 1704303.
(27) Park, K. S.; Ni, Z.; Côté, A. P.; Choi, J. Y.; Huang, R.; Uribe-Romo, F. J.; Chae, H. K.; O'Keeffe, M.; Yaghi, O. M. Exceptional chemical and thermal stability of zeolitic imidazolate frameworks. *Proc. Natl. Acad. Sci. U. S. A.* **2006**, *103* (27), 10186−10191.
(28) Li, X.; Liu, J.; Zhou, K.; Ullah, S.; Wang, H.; Zou, J.; Thonhauser, T.; Li, J. Tuning Metal-Organic Framework (MOF) Topology by Regulating Ligand and Secondary Building Unit (SBU) Geometry: Structures Built on 8-Connected M_6 (M = Zr, Y) Clusters and a Flexible Tetracarboxylate for Propane-Selective Propane/Propylene Separation. *J. Am. Chem. Soc.* **2022**, *144* (47), 21702−21709.
(29) Shao, K.; Wen, H.; Liang, C.; Xiao, X.; Gu, X.; Chen, B.; Qian, G.; Li, B. Engineering Supramolecular Binding Sites in a Chemically Stable Metal-Organic Framework for Simultaneous High C_2H_2 Storage and Separation. *Angew. Chem., Int. Ed.* **2022**, *61* (41), No. e202211523.
(30) Zhang, F.; Shang, H.; Zhai, B.; Zhao, Z.; Wang, Y.; Li, L.; Li, J.; Yang, J. Synergistic Nitrogen Binding Sites in a Metal-Organic Framework for Efficient N_2/O_2 Separation. *Angew. Chem., Int. Ed.* **2023**, *62* (50), No. e202316149.
(31) Wang, H.; Shi, Z.; Yang, J.; Sun, T.; Rungtaweevoranit, B.; Lyu, H.; Zhang, Y. B.; Yaghi, O. M. Docking of Cu^I and Ag^I in Metal-Organic Frameworks for Adsorption and Separation of Xenon. *Angew. Chem., Int. Ed.* **2021**, *60* (7), 3417−3421.
(32) Lyu, H.; Chen, O. I.-F.; Hanikel, N.; Hossain, M. I.; Flaig, R. W.; Pei, X.; Amin, A.; Doherty, M. D.; Impastato, R. K.; Glover, T. G.; Moore, D. R.; Yaghi, O. M. Carbon Dioxide Capture Chemistry of Amino Acid Functionalized Metal-Organic Frameworks in Humid Flue Gas. *J. Am. Chem. Soc.* **2022**, *144* (5), 2387−2396.
(33) Zhang, L.; Wang, J.; Jiang, K.; Xiao, Z.; Gao, Y.; Lin, S.; Chen, B. Self-Reconstructed Metal−Organic Framework Heterojunction for Switchable Oxygen Evolution Reaction. *Angew. Chem., Int. Ed.* **2022**, *61* (51), No. e202214794.
(34) Eagleton, A. M.; Ko, M.; Stolz, R. M.; Vereshchuk, N.; Meng, Z.; Mendecki, L.; Levenson, A. M.; Huang, C.; MacVeagh, K. C.; Mahdavi-Shakib, A.; Mahle, J. J.; Peterson, G. W.; Frederick, B. G.; Mirica, K. A. Fabrication of Multifunctional Electronic Textiles Using Oxidative Restructuring of Copper into a Cu-Based Metal-Organic Framework. *J. Am. Chem. Soc.* **2022**, *144* (51), 23297−23312.
(35) Geng, J.; Ni, Y.; Zhu, Z.; Wu, Q.; Gao, S.; Hua, W.; Indris, S.; Chen, J.; Li, F. Reversible Metal and Ligand Redox Chemistry in Two-Dimensional Iron−Organic Framework for Sustainable Lithium-Ion Batteries. *J. Am. Chem. Soc.* **2023**, *145* (3), 1564−1571.
(36) Yang, M.; Zeng, X.; Xie, M.; Wang, Y.; Xiao, J.-M.; Chen, R.-H.; Yi, Z.-J.; Huang, Y.-F.; Bin, D.-S.; Li, D. Conductive Metal-Organic Framework with Superior Redox Activity as a Stable High-Capacity Anode for High-Temperature K-Ion Batteries. *J. Am. Chem. Soc.* **2024**, *146* (10), 6753−6762.
(37) Sun, L.; Zhu, C.; Li, L.; Zheng, R.; Yuan, J.; Li, Z.; Sun, J.; Sheng, G.; Wu, H. Design of Ligand-Nonbridging Sites in Metal-

https://doi.org/10.1021/jacs.5c16469
J. Am. Chem. Soc. XXXX, XXX, XXX−XXX

Organic Frameworks for Boosting Lithium Storage Capacity. *Angew. Chem., Int. Ed.* **2024**, *64* (6), No. e202418031.
(38) Zheng, Z.; Nguyen, H. L.; Hanikel, N.; Li, K. K.-Y.; Zhou, Z.; Ma, T.; Yaghi, O. M. High-yield, green and scalable methods for producing MOF-303 for water harvesting from desert air. *Nat. Protoc.* **2023**, *18* (1), 136−156.
(39) Xu, K.; Liang, L.; Li, T.; Bao, M.; Yu, Z.; Wang, J.; Thalluri, S. M.; Lin, F.; Liu, Q.; Cui, Z.; Song, S.; Liu, L. $Pt_{1.8}Pd_{0.2}CuGa$ Intermetallic Nanocatalysts with Enhanced Methanol Oxidation Performance for Efficient Hybrid Seawater Electrolysis. *Adv. Mater.* **2024**, *36* (31), 2403792.
(40) Zheng, Z.; Hanikel, N.; Lyu, H.; Yaghi, O. M. Broadly Tunable Atmospheric Water Harvesting in Multivariate Metal-Organic Frameworks. *J. Am. Chem. Soc.* **2022**, *144* (49), 22669−22675.
(41) Jiang, H.; Liu, X.-C.; Wu, Y.; Shu, Y.; Gong, X.; Ke, F.-S.; Deng, H. Metal-Organic Frameworks for High Charge-Discharge Rates in Lithium-Sulfur Batteries. *Angew. Chem., Int. Ed.* **2018**, *57* (15), 3916−3921.
(42) Zeng, Q.; Li, X.; Gong, W.; Guo, S.; Ouyang, Y.; Li, D.; Xiao, Y.; Tan, C.; Xie, L.; Lu, H.; Zhang, Q.; Huang, S. Copolymerization of Sulfur Chains with Vinyl Functionalized Metal-Organic Framework for Accelerating Redox Kinetics in Lithium-Sulfur Batteries. *Adv. Energy Mater.* **2022**, *12* (21), 2104074.
(43) Yang, D.; Liang, Z.; Tang, P.; Zhang, C.; Tang, M.; Li, Q.; Biendicho, J. J.; Li, J.; Heggen, M.; Dunin-Borkowski, R. E.; Xu, M.; Llorca, J.; Arbiol, J.; Morante, J. R.; Chou, S.; Cabot, A. A High Conductivity 1D π-d Conjugated Metal-Organic Framework with Efficient Polysulfide Trapping−Diffusion−Catalysis in Lithium-Sulfur Batteries. *Adv. Mater.* **2022**, *34* (10), 2108835.
(44) Demir-Cakan, R.; Morcrette, M.; Nouar, F.; Davoisne, C.; Devic, T.; Gonbeau, D.; Dominko, R.; Serre, C.; Férey, G.; Tarascon, J.-M. Cathode Composites for Li−S Batteries via the Use of Oxygenated Porous Architectures. *J. Am. Chem. Soc.* **2011**, *133* (40), 16154−16160.
(45) Li, Z.; Li, P.; Meng, X.; Lin, Z.; Wang, R. The Interfacial Electronic Engineering in Binary Sulfiphilic Cobalt Boride Heterostructure Nanosheets for Upgrading Energy Density and Longevity of Lithium-Sulfur Batteries. *Adv. Mater.* **2021**, *33* (42), 2102338.
(46) Bai, S.; Liu, X.; Zhu, K.; Wu, S.; Zhou, H. Metal−organic framework-based separator for lithium−sulfur batteries. *Nat. Energy* **2016**, *1* (7), 16094.
(47) Luo, C.; Xu, G.-L.; Ji, X.; Hou, S.; Chen, L.; Wang, F.; Jiang, J.; Chen, Z.; Ren, Y.; Amine, K.; Wang, C. Reversible Redox Chemistry of Azo Compounds for Sodium-Ion Batteries. *Angew. Chem.* **2018**, *130* (11), 2929−2933.
(48) Luo, C.; Borodin, O.; Ji, X.; Hou, S.; Gaskell, K. J.; Fan, X.; Chen, J.; Deng, T.; Wang, R.; Jiang, J.; Wang, C. Azo compounds as a family of organic electrode materials for alkali-ion batteries. *Proc. Natl. Acad. Sci. U. S. A.* **2018**, *115* (9), 2004−2009.
(49) Luo, C.; Ji, X.; Chen, J.; Gaskell, K. J.; He, X.; Liang, Y.; Jiang, J.; Wang, C. Solid-State Electrolyte Anchored with a Carboxylated Azo Compound for All−Solid−State Lithium Batteries. *Angew. Chem., Int. Ed.* **2018**, *57* (28), 8567−8571.
(50) Zu, X.; Zhang, L.; Qian, Y.; Zhang, C.; Yu, G. Molecular Engineering of Azobenzene-Based Anolytes Towards High-Capacity Aqueous Redox Flow Batteries. *Angew. Chem., Int. Ed.* **2020**, *59* (49), 22163−22170.
(51) Das, G.; Prakasam, T.; Addicoat, M. A.; Sharma, S. K.; Ravaux, F.; Mathew, R.; Baias, M.; Jagannathan, R.; Olson, M. A.; Trabolsi, A. Azobenzene-Equipped Covalent Organic Framework: Light-Operated Reservoir. *J. Am. Chem. Soc.* **2019**, *141* (48), 19078−19087.
(52) Zhou, Z. B.; Tian, P. J.; Yao, J.; Lu, Y.; Qi, Q. Y.; Zhao, X. Toward azo-linked covalent organic frameworks by developing linkage chemistry via linker exchange. *Nat. Commun.* **2022**, *13*, 2180.
(53) Andjaba, J. M.; Rybak, C. J.; Wang, Z.; Ling, J.; Mei, J.; Uyeda, C. Catalytic Synthesis of Conjugated Azopolymers from Aromatic Diazides. *J. Am. Chem. Soc.* **2021**, *143* (10), 3975−3982.
(54) Bai, Q.; Huang, J.; Tang, K.; Zhu, Y.; Wu, D. Arylamine-Linked Porous Organic Polymers with Abundant Redox−Active Sites as High−Capacity and High−Rate Organic Cathodes for Lithium-Ion Batteries. *Adv. Mater.* **2025**, 2416661.
(55) Feng, W.; Yang, Z.; Guo, C.; Zhuang, H.; Xu, R.; Zhang, H.; Shi, M.; Chen, Z.; Chen, Y.; Lan, Y. Three-Motif Molecular Junction Covalent Organic Frameworks for Symmetric All-Organic Lithium-Ion Battery. *Angew. Chem., Int. Ed.* **2025**, No. e202508937.
(56) Ye, C.; Zhou, X.; Tang, S. An Azo Polymer with Abundant Active Sites and Extended Conjugation as a Stable Cathode for High-Performance Zinc−Organic Batteries. *Angew. Chem., Int. Ed.* **2025**, No. e202501743.
(57) Cornell, H. D.; Sose, A. T.; Ilic, S.; Chinnabattigalla, S.; Lidman, N. E.; Oldmixon, C. M.; Yang, X.; Deshmukh, S. A.; Morris, A. J. Photoactivated Multivariate Metal-Organic Frameworks for On-Demand Drug Release: The Role of Host-Guest Interactions. *J. Am. Chem. Soc.* **2025**, *147* (9), 7423−7432.
(58) Zhang, M.; Chen, Y.-P.; Bosch, M.; Gentle, T.; Wang, K.; Feng, D.; Wang, Z. U.; Zhou, H.-C. Symmetry-Guided Synthesis of Highly Porous Metal-Organic Frameworks with Fluorite Topology. *Angew. Chem., Int. Ed.* **2014**, *53* (3), 815−818.
(59) Wang, Y.; Liu, Q.; Zhang, Q.; Peng, B.; Deng, H. Molecular Vise Approach to Create Metal-Binding Sites in MOFs and Detection of Biomarkers. *Angew. Chem., Int. Ed.* **2018**, *57* (24), 7120−7125.
(60) Yan, W.; Li, S.; Yang, T.; Xia, Y.; Zhang, X.; Wang, C.; Yan, Z.; Deng, F.; Zhou, Q.; Deng, H. Molecular Vises for Precisely Positioning Ligands near Catalytic Metal Centers in Metal-Organic Frameworks. *J. Am. Chem. Soc.* **2020**, *142* (38), 16182−16187.
(61) Pang, J.; Yuan, S.; Du, D.; Lollar, C.; Zhang, L.; Wu, M.; Yuan, D.; Zhou, H.-C.; Hong, M. Flexible Zirconium MOFs as Bromine-Nanocontainers for Bromination Reactions under Ambient Conditions. *Angew. Chem., Int. Ed.* **2017**, *56* (46), 14622−14626.
(62) Wang, L.; Ghoussoub, M.; Wang, H.; Shao, Y.; Sun, W.; Tountas, A. A.; Wood, T. E.; Li, H.; Loh, J. Y. Y.; Dong, Y.; Xia, M.; Li, Y.; Wang, S.; Jia, J.; Qiu, C.; Qian, C.; Kherani, N. P.; He, L.; Zhang, X.; Ozin, G. A. Photocatalytic Hydrogenation of Carbon Dioxide with High Selectivity to Methanol at Atmospheric Pressure. *Joule* **2018**, *2* (7), 1369−1381.
(63) Sun, L.; Li, R.; Zhan, W.; Yuan, Y.; Wang, X.; Han, X.; Zhao, Y. Double-shelled hollow rods assembled from nitrogen/sulfur-codoped carbon coated indium oxide nanoparticles as excellent photocatalysts. *Nat. Commun.* **2019**, *10* (1), 2270.
(64) Wang, P.; Sun, F.; Xiong, S.; Zhang, Z.; Duan, B.; Zhang, C.; Feng, J.; Xi, B. WSe_2 Flakelets on N-Doped Graphene for Accelerating Polysulfide Redox and Regulating Li Plating. *Angew. Chem., Int. Ed.* **2021**, *61* (7), No. e202116048.
(65) Zhao, C.; Liu, Y.; Huo, F.; Guo, Z.; Lu, Y.; Sun, B.; Li, M.; Xu, H.; Zhang, M.; Fan, H.; Sun, Z.; Cabot, A.; Zhang, Y. Synergistic Catalysts for Lithium-Sulfur Batteries: Ni Single Atom and MoC Nanoclusters Composites. *Angew. Chem., Int. Ed.* **2025**, No. e202502177.
(66) Huang, Y.; Li, J.; Zhang, Y.; Lin, L.; Sun, Z.; Gao, G.; Sa, B.; Wang, L.; Ma, L.; Lee, S.; Wang, M.-S.; Peng, D.-L.; Amine, K.; Xie, Q. Energizing Robust Sulfur/Lithium Electrochemistry via Nanoscale-Asymmetric-Size Synergism. *J. Am. Chem. Soc.* **2025**, *147* (6), 4752−4765.
(67) Zhou, G.; Tian, H.; Jin, Y.; Tao, X.; Liu, B.; Zhang, R.; Seh, Z. W.; Zhuo, D.; Liu, Y.; Sun, J.; Zhao, J.; Zu, C.; Wu, D. S.; Zhang, Q.; Cui, Y. Catalytic oxidation of Li_2S on the surface of metal sulfides for Li−S batteries. *Proc. Natl. Acad. Sci. U. S. A.* **2017**, *114* (5), 840−845.
(68) Li, H.; Shi, P.; Wang, L.; Yan, T.; Guo, T.; Xia, X.; Chen, C.; Mao, J.; Sun, D.; Zhang, L. Cooperative Catalysis of Polysulfides in Lithium-Sulfur Batteries through Adsorption Competition by Tuning Cationic Geometric Configuration of Dual−active Sites in Spinel Oxides. *Angew. Chem., Int. Ed.* **2023**, *62*, No. e202216286.
(69) Xu, J.; An, S.; Song, X.; Cao, Y.; Wang, N.; Qiu, X.; Zhang, Y.; Chen, J.; Duan, X.; Huang, J.; Li, W.; Wang, Y. Towards High Performance Li−S Batteries via Sulfonate-Rich COF−Modified Separator. *Adv. Mater.* **2021**, *33* (49), 2105178.
(70) Zuo, X.; Wang, L.; Zhen, M.; You, T.; Liu, D.; Zhang, Y. Multifunctional TiN−MXene−Co@CNTs Networks as Sulfur/

https://doi.org/10.1021/jacs.5c16469
J. Am. Chem. Soc. XXXX, XXX, XXX−XXX

Lithium Host for High−Areal−Capacity Lithium-Sulfur Batteries. *Angew. Chem., Int. Ed.* **2024**, *63* (35), No. e202408026.
(71) Hao, G.; Tang, C.; Zhang, E.; Zhai, P.; Yin, J.; Zhu, W.; Zhang, Q.; Kaskel, S. Thermal Exfoliation of Layered Metal-Organic Frameworks into Ultrahydrophilic Graphene Stacks and Their Applications in Li−S Batteries. *Adv. Mater.* **2017**, *29* (37), 1702829.
(72) Baumann, A. E.; Han, X.; Butala, M. M.; Thoi, V. S. Lithium Thiophosphate Functionalized Zirconium MOFs for Li−S Batteries with Enhanced Rate Capabilities. *J. Am. Chem. Soc.* **2019**, *141* (44), 17891−17899.
(73) Tao, A.; Zhang, K.; Ma, X.; Song, X.; Liang, J.; Wang, Y.; Liu, Y.; Jin, L.; Tie, Z.; Jin, Z. Building Lithium-Polycarbonsulfide Batteries with High Energy Density and Long Cycling Life. *ACS Energy Lett.* **2023**, *8* (1), 79−89.
(74) Lv, S.; Ma, X.; Ke, S.; Wang, Y.; Ma, T.; Yuan, S.; Jin, Z.; Zuo, J.-L. Metal-Coordinated Covalent Organic Frameworks as Advanced Bifunctional Hosts for Both Sulfur Cathodes and Lithium Anodes in Lithium-Sulfur Batteries. *J. Am. Chem. Soc.* **2024**, *146* (13), 9385−9394.
(75) Zhu, J.; Xian, Y.; Liang, F.; Lin, C.; He, H.; Wang, N.; Huang, D.; Zhu, Y. Optimizing Electron Modulation Induced by the Interfacial Coupling in Cu_3P-Cu_2O Heterostructures to Enhance Polysulfide Conversion. *Adv. Funct. Mater.* **2025**, *35* (26), 2425945.
(76) Peng, H.-J.; Zhang, Z.-W.; Huang, J.-Q.; Zhang, G.; Xie, J.; Xu, W.-T.; Shi, J.-L.; Chen, X.; Cheng, X.-B.; Zhang, Q. A Cooperative Interface for Highly Efficient Lithium-Sulfur Batteries. *Adv. Mater.* **2016**, *28* (43), 9551−9558.
(77) Wang, Y.; Zhang, R.; Chen, J.; Wu, H.; Lu, S.; Wang, K.; Li, H.; Harris, C. J.; Xi, K.; Kumar, R. V.; Ding, S. Enhancing Catalytic Activity of Titanium Oxide in Lithium-Sulfur Batteries by Band Engineering. *Adv. Energy Mater.* **2019**, *9* (24), 1900953.
(78) Li, T.; Shi, K.; Li, X.; Huang, W.; Li, J.; Li, J.; Wang, K.; Deng, Y.; Chen, H.; Min, Y.; Li, J.; Liu, Q. Electron Filling Control Mechanism Triggered by the Penetration Effect in Fe_3N/Fe Accelerates Sulfur Redox Kinetics. *Adv. Funct. Mater.* **2025**, 2505615.
(79) Li, J.; Wang, Z.; Shi, K.; Wu, Y.; Huang, W.; Min, Y.; Liu, Q.; Liang, Z. Nanoreactors Encapsulating Built-in Electric Field as a "Bridge" for Li−S Batteries: Directional Migration and Rapid Conversion of Polysulfides. *Adv. Energy Mater.* **2023**, *14* (9), 2303546.
(80) Du, Z.; Chen, X.; Hu, W.; Chuang, C.; Xie, S.; Hu, A.; Yan, W.; Kong, X.; Wu, X.; Ji, H.; Wan, L.-J. Cobalt in Nitrogen-Doped Graphene as Single-Atom Catalyst for High-Sulfur Content Lithium-Sulfur Batteries. *J. Am. Chem. Soc.* **2019**, *141* (9), 3977−3985.

https://doi.org/10.1021/jacs.5c16469
J. Am. Chem. Soc. XXXX, XXX, XXX−XXX